

Stress attractors predicted by a high-cycle accumulation model confirmed by undrained cyclic triaxial tests

T. Wichtmannⁱ⁾ Th. Triantafyllidisⁱⁱ⁾

Abstract: Depending on the boundary conditions a high-cyclic loading (= large number of cycles $N \geq 10^3$, small strain amplitudes $\varepsilon^{\text{ampl}} \leq 10^{-3}$) may either lead to strain accumulation or stress relaxation in the soil. This paper concentrates on stress relaxation. For a cyclic loading applied under undrained triaxial conditions, the high-cycle accumulation (HCA) model of Niemunis et al. [23] predicts a relaxation of average effective stress until a stress ratio $\eta^{\text{av}} = q^{\text{av}}/p^{\text{av}} = M_{cc}$ (triaxial compression) or M_{ec} (extension) is reached. M_{cc} and M_{ec} are very similar to the critical stress ratios M_c and M_e known from monotonic shear tests. The average effective stresses finally reached after a sufficiently large number of cycles are called "stress attractors" herein. A zero effective stress state (liquefaction, $p^{\text{av}} = q^{\text{av}} = 0$) is obtained as a special case of a stress attractor. However, up to now the stress attractors predicted by the HCA model were based on the data from drained cyclic tests only. In the present study they have been approximately confirmed by stress relaxation experiments, i.e. undrained cyclic triaxial tests with stress or strain control. These tests have been performed on a fine sand, varying the initial values of density, mean pressure and stress ratio as well as the stress or strain amplitude.

Keywords: High-cycle accumulation (HCA) model, undrained cyclic tests, fine sand, stress relaxation, stress attractors

1 Introduction

High-cycle accumulation (HCA) models [1, 17, 23, 26, 31] have been primarily developed in order to predict the permanent deformations in soils due to a cyclic loading with many cycles ($N \geq 10^3$) of small to intermediate strain amplitudes ($\varepsilon^{\text{ampl}} \leq 10^{-3}$). These models can be applied to predict the long-term settlements of foundations subjected to traffic loading (e.g. high-speed railways, magnetic levitation trains), wind and wave action (e.g. onshore and offshore wind power plants [45, 52], coastal structures) or repeated filling and emptying processes (e.g. tanks, silos, watergates). Machine foundations (e.g. gas turbines [6]) are another practical example for a high-cyclic loading.

However, if some or all components of the strain tensor are fully or partly restricted, beside the accumulation of strain also a relaxation of stress takes place in the soil. Such stress relaxation occurs in many boundary value problems with high-cyclic loading, e.g. in the case of monopile foundations for offshore wind power plants which are subjected to horizontal wind and wave loading [45]. In that case a considerable redistribution of the horizontal stresses acting on the pile shaft may occur, in particular in the upper layers of soil. A redistribution of stress due to high-cyclic loading has been also observed for shallow foundations supporting a relatively rigid structure [44, 52]. If some of the foundations are subjected to cycles with larger amplitudes and thus suffer larger accumulation, the average foundation stresses are redistributed towards the foundations with lower cyclic loads. Accordingly, the internal forces in the structure are altered, probably leading to damage.

Consequently, a HCA model must also properly describe the stress relaxation in the soil caused by the cyclic load-

ing. As discussed in detail in the next Section, the stress relaxation predicted by the HCA model of Niemunis et al. [23] depends on the *intensity* of strain accumulation $\dot{\varepsilon}^{\text{acc}}$, the *direction* of accumulation (cyclic flow rule, volumetric component m_v , deviatoric component m_q) and the elastic stiffness (bulk modulus K , shear modulus G). The quantities $\dot{\varepsilon}^{\text{acc}}$ and K , G determine the *intensity* of stress relaxation [41]. The *stress attractors*, i.e. the average effective stresses reached by the relaxation path after a sufficiently large number of cycles, come out of the equations for the cyclic flow rule. According to these equations, for triaxial conditions the HCA model predicts a stress relaxation until the stress ratio $\eta^{\text{av}} = q^{\text{av}}/p^{\text{av}}$ is equal to the parameter M of the cyclic flow rule ($M = M_{cc}$ for triaxial compression, $M = M_{ec}$ for extension).

The parameter M used in the HCA model is usually calibrated from a series of drained cyclic tests with different average stress ratios [39, 42]. Figure 1 presents the results of such a test series performed on the fine sand ($d_{50} = 0.14$ mm, $C_u = 1.5$, $e_{\text{min}} = 0.677$, $e_{\text{max}} = 1.054$) used in the present study. In those tests, medium dense samples with $I_{D0} = (e_{\text{max}} - e)/(e_{\text{max}} - e_{\text{min}}) = 0.57 \div 0.62$ were subjected to 10^5 cycles. The average mean pressure was $p^{\text{av}} = 200$ kPa and the stress amplitude was $q^{\text{ampl}} = 40$ kPa in all tests. Stress ratios η^{av} between 0.5 and 1.25 were tested. While Figure 1a presents the curves of accumulated strain ε^{acc} (with $\varepsilon = \sqrt{(\varepsilon_1)^2 + 2(\varepsilon_3)^2}$) versus the number of cycles N , the accumulated deviatoric strain $\varepsilon_q^{\text{acc}}$ is plotted versus the accumulated volumetric strain $\varepsilon_v^{\text{acc}}$ in Figure 1b, with $\varepsilon_v = \varepsilon_1 + 2\varepsilon_3$ and $\varepsilon_q = 2/3(\varepsilon_1 - \varepsilon_3)$. The parameter M used in the cyclic flow rule corresponds to the average stress ratio η^{av} for which the accumulation is purely deviatoric, i.e. no volumetric strain accumulation takes place at that stress ratio ($\dot{\varepsilon}_v^{\text{acc}} = 0$). From the data in Figure 1b, a value $M = M_{cc} = 1.25$ can be derived, corresponding to a critical friction angle of $\varphi_{cc} = 31.1^\circ$. The corresponding lines in the

ⁱ⁾Researcher, Institute of Soil Mechanics and Rock Mechanics (IBF), Karlsruhe Institute of Technology (KIT), Germany (corresponding author). Email: torsten.wichtmann@kit.edu

ⁱⁱ⁾Professor and Director of the IBF, KIT, Germany

p - q plane, inclined by M_{cc} for triaxial compression or M_{ec} for triaxial extension, are denoted as "zero volumetric accumulation (drained)" lines (ZVADL) in the following. The M_{cc} value obtained from Figure 1b is in good accordance with the literature [3, 22, 39, 42]. Note, that the parameters M_{cc} and M_{ec} used in the HCA model are similar but need not be identical to the critical stress ratios M_c and M_e obtained from monotonic shear tests [42]. Therefore, the ZVADL lies close to the critical state line (CSL) from monotonic tests.

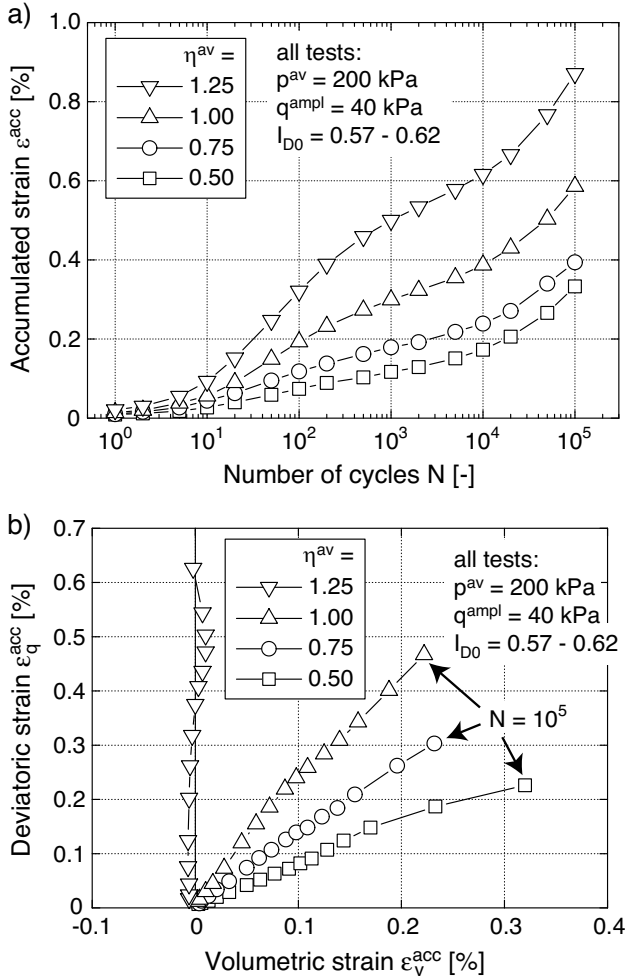


Fig. 1: a) Strain accumulation curves $\varepsilon^{acc}(N)$ and b) accumulated deviatoric strain ε_q^{acc} versus accumulated volumetric strain ε_v^{acc} measured in drained cyclic triaxial tests on the fine sand with different average stress ratios η^{av}

The stress relaxation predicted by the HCA model proceeds until the average effective stress path reaches the ZVADL. However, the assumption of the ZVADL as a stress attractor is only based on drained cyclic test data as that shown in Figure 1b. Up to now this assumption has been confirmed in stress relaxation experiments for special cases only, i.e. for triaxial test conditions leading to a zero effective stress state (liquefaction, $p^{av} = q^{av} = 0$) after a sufficiently large number of cycles. The ZVADL as a stress attractor can be checked by undrained (constant volume) triaxial tests with stress cycles applied at an average stress ratio $\eta^{av} > 0$. Such examination is the purpose of the experimental study documented in this paper.

All samples (diameter $d = 100$ mm, height $h = 100$

mm) were prepared by air pluviation and tested under fully water-saturated conditions. The loading was applied very slowly (displacement rate 0.05 mm/min) by a load press driven by an electrical motor, controlling the minimum and maximum stresses.

2 Prediction of strain accumulation or stress relaxation by the HCA model

In the following, the prediction of strain accumulation or stress relaxation by the HCA model is recapitulated for the simple boundary value problem of an axisymmetric triaxial test. For axisymmetric element tests it is convenient to write the basic equations of the HCA model with Roscoe's invariants:

$$\dot{p} = K (\dot{\varepsilon}_v - \dot{\varepsilon}^{acc} m_v) \quad (1)$$

$$\dot{q} = 3G (\dot{\varepsilon}_q - \dot{\varepsilon}^{acc} m_q) \quad (2)$$

In contrast to conventional constitutive models, HCA models predict only the cumulative portions of stress or strain. Therefore, in the context of HCA models the dot over a symbol means a derivative with respect to the number of cycles N (instead of time t), i.e. $\dot{\square} = \partial \square / \partial N$ or an increment per cycle. In Eqs. (1) and (2), the rates of mean pressure $\dot{p} = (\dot{\sigma}_1 + 2\dot{\sigma}_3)/3$ and deviatoric stress $\dot{q} = \dot{\sigma}_1 - \dot{\sigma}_3$ are inter-related with the rates of volumetric strain $\dot{\varepsilon}_v$ and deviatoric strain $\dot{\varepsilon}_q$ by an elastic stiffness described by bulk modulus $K = E/3/(1 - 2\nu)$ and shear modulus $G = E/2/(1 + \nu)$. Omitting the plastic strain rate (see [23]) in Eqs. (1) and (2) is legitimate for homogeneous stress fields.

The intensity of accumulation ε^{acc} is calculated as the product of six functions, considering the influences of strain amplitude, void ratio, average stress, cyclic preloading and polarization changes [23, 38, 40]. The equations for the volumetric (m_v) and deviatoric (m_q) portions of the cyclic flow rule are adapted from the Modified Cam Clay (MCC) model [39, 42]:

$$m_v = f \left[1 - \frac{(\eta^{av})^2}{M^2} \right] \quad (3)$$

$$m_q = 2 f \frac{\eta^{av}}{M^2} \quad (4)$$

with

$$f = \frac{1}{\sqrt{\frac{1}{3} \left[1 - \frac{(\eta^{av})^2}{M^2} \right]^2 + 6 \left(\frac{\eta^{av}}{M^2} \right)^2}} \quad (5)$$

$$M = FM_{cc} \quad (6)$$

$$F = \begin{cases} 1 + M_{ec}/3 & \text{for } \eta^{av} \leq M_{ec} \\ 1 + \eta^{av}/3 & \text{for } M_{ec} < \eta^{av} < 0 \\ 1 & \text{for } \eta^{av} \geq 0 \end{cases} \quad (7)$$

wherein

$$M_{cc} = \frac{6 \sin \varphi_{cc}}{3 - \sin \varphi_{cc}} \quad \text{and} \quad M_{ec} = -\frac{6 \sin \varphi_{cc}}{3 + \sin \varphi_{cc}}. \quad (8)$$

φ_{cc} is a friction angle corresponding to the critical friction angle φ_c from monotonic shear tests.

Eqs. (3) and (4) can be used to calculate the ratio of the rates of volumetric and deviatoric strain accumulation

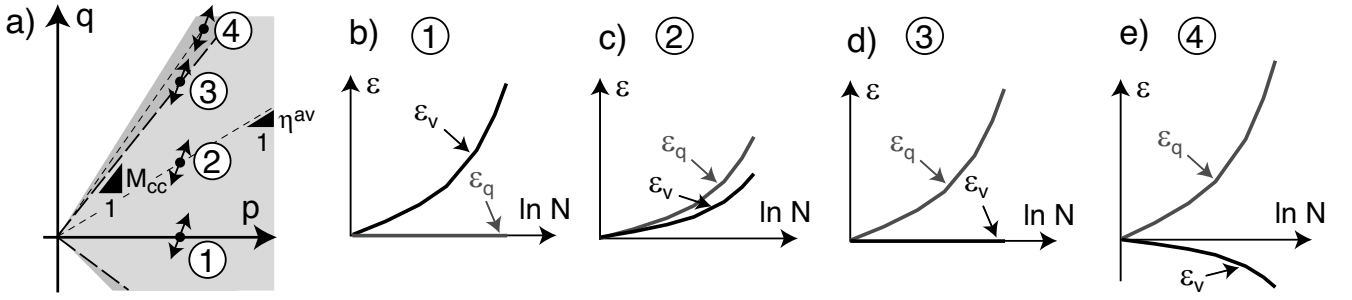


Fig. 2: Strain accumulation predicted by the HCA model for different average stress ratios in drained cyclic triaxial tests

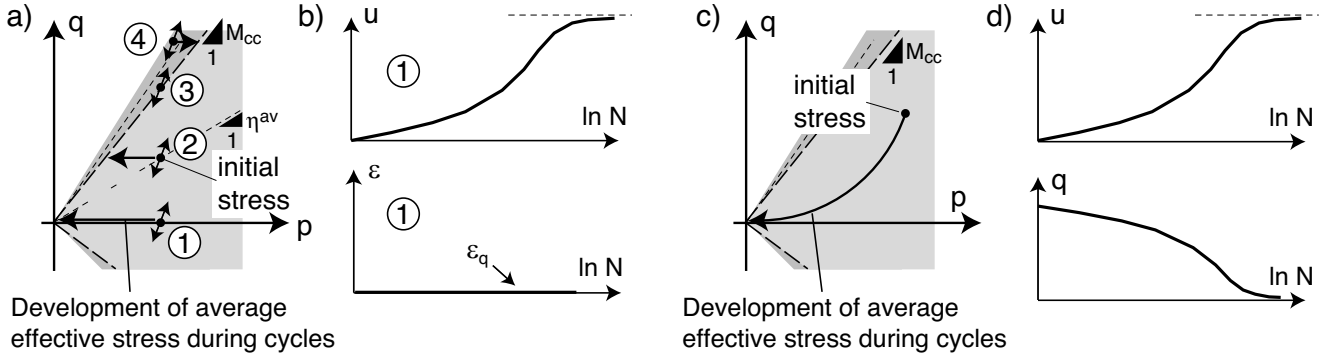


Fig. 3: Development of average stress and shear strain accumulation predicted by the HCA model for undrained triaxial tests with different control: a-b) stress cycles, c-d) strain cycles

predicted by the HCA model for a drained test with stress-controlled cycles:

$$\frac{\dot{\varepsilon}_v^{\text{acc}}}{\dot{\varepsilon}_q^{\text{acc}}} = \frac{m_v}{m_q} = \frac{M^2 - (\eta^{\text{av}})^2}{2\eta^{\text{av}}} \quad (9)$$

Depending on the boundary conditions, the basic equations (1) and (2) predict either a change of the average effective stress or an accumulation of permanent strain or both. Furthermore, according to Eqs. (3) and (4), the portions of volumetric and shear strain accumulation ($\dot{\varepsilon}_v^{\text{acc}}/\dot{\varepsilon}_q^{\text{acc}}$) or isotropic and deviatoric stress relaxation (\dot{p}/\dot{q}) depend on the average stress ratio η^{av} .

In a drained cyclic triaxial test with stress cycles an unconstrained accumulation of strain takes place. The average stress does not change during the cycles, i.e. $\dot{p} = 0$ and $\dot{q} = 0$ holds. In that case, the basic equations (1) and (2) simplify to:

$$\dot{\varepsilon}_v = \dot{\varepsilon}^{\text{acc}} m_v \quad \text{and} \quad \dot{\varepsilon}_q = \dot{\varepsilon}^{\text{acc}} m_q \quad (10)$$

The four cases of stress cycles shown in the p - q -plane in Figure 2a are considered in the following. For an axial cyclic loading the stress paths have an inclination of 1:3 in the p - q -plane. In case "1" the average effective stress is isotropic ($\eta^{\text{av}} = 0$). The components of the direction of accumulation are obtained from Eqs. (3) and (4):

$$m_v = \sqrt{3} \quad \text{and} \quad m_q = 0 \quad (11)$$

From Eq. (10) follows:

$$\dot{\varepsilon}_v = \sqrt{3} \dot{\varepsilon}^{\text{acc}} \quad \text{and} \quad \dot{\varepsilon}_q = 0 \quad (12)$$

As shown schematically in Figure 2b, a pure volumetric accumulation of strain is predicted. No accumulation of shear

deformation takes place. If the cycles are applied at an average stress ratio $\eta^{\text{av}} = M_{cc}$ (case "3" in Figure 2a), the components of the direction of accumulation read:

$$m_v = 0 \quad \text{and} \quad m_q = \sqrt{2/3} \quad (13)$$

leading to the strain accumulation rates

$$\dot{\varepsilon}_v = 0 \quad \text{and} \quad \dot{\varepsilon}_q = \sqrt{2/3} \dot{\varepsilon}^{\text{acc}} \quad (14)$$

In that case only the shear strain accumulates while the volumetric strain does not change (see the scheme in Figure 2d). For stress ratios $0 < \eta^{\text{av}} < M_{cc}$ (case "2", Figure 2c) the equations of the HCA model predict an accumulation of both, permanent volume and shear strains. Their ratio depends on η^{av} . In the overcritical regime $\eta^{\text{av}} > M_{cc}$ (case "4", Figure 2e) the expression for the volumetric strain accumulation rate becomes negative, i.e. cumulative dilatancy is predicted. The tests in [37–39, 42] confirm the strain accumulation behaviour shown schematically in Figure 2.

An example with a partly prevented accumulation of deformation is the undrained triaxial test with axial stress cycles performed on fully water-saturated samples. The volume changes are zero ($\dot{\varepsilon}_v = 0$) if membrane penetration effects and the compressibility of water are disregarded. The average value of deviatoric stress stays constant during the cycles, i.e. $\dot{q} = 0$ holds. The basic equations (1) and (2) then simplify to:

$$\dot{p} = -K \dot{\varepsilon}^{\text{acc}} m_v = -\dot{u} \quad (15)$$

$$\dot{\varepsilon}_q = \dot{\varepsilon}^{\text{acc}} m_q, \quad (16)$$

i.e. they describe a relaxation \dot{p} of the effective mean pressure p and an accumulation $\dot{\varepsilon}_q$ of shear strain. The rate of pore water pressure accumulation \dot{u} can be calculated from

the relationship $\dot{u} = -\dot{p}$. Similar to the drained case, the split-up of the rate of accumulation into a deviatoric part (permanent shear strain) and an isotropic portion (relaxation of effective mean pressure / pore water pressure accumulation) depends on the average stress ratio. The soil response in the undrained cyclic test is adequately described by the schemes in Figure 2 if ε_v is replaced by u . For the special case of an isotropic initial stress, one obtains:

$$\dot{u} = \sqrt{3} K \dot{\varepsilon}^{\text{acc}} \quad \text{and} \quad \dot{\varepsilon}_q = 0, \quad (17)$$

which is shown schematically as case "1" in Figure 3a,b. While in the drained case the accumulation of volumetric strain is only restricted by the maximum packing density, for the undrained tests with stress ratios $0 < \eta^{\text{av}} < M_{cc}$ the HCA model predicts a relaxation of effective mean pressure that stops if the stress ratio $\eta^{\text{av}} = M_{cc}$, i.e. the ZVADL is reached (case "2" in Figure 3a). For $\eta^{\text{av}} = M_{cc}$ (case "3") no pore water pressure accumulation takes place. For overcritical stress ratios (case "4") negative rates \dot{u} can be expected. Tests of the type shown as case "2" in Figure 3a have been performed in the framework of the experimental study discussed in this paper.

A boundary value problem with fully prevented strain accumulation is the undrained triaxial test with strain cycles applied in the axial direction. In that case $\dot{\varepsilon}_v = 0$, $\dot{\varepsilon}_q = 0$ and $\dot{\varepsilon}_1 = 0$ holds. The basic equations (1) and (2) simplify to:

$$\dot{p} = -K \dot{\varepsilon}^{\text{acc}} m_v \quad (18)$$

$$\dot{q} = -3G \dot{\varepsilon}^{\text{acc}} m_q \quad (19)$$

Therefore, the cyclic loading leads to a relaxation of both, the average effective mean pressure p and the average deviatoric stress q (Figure 3d). The HCA model predicts effective stress paths as shown schematically in Figure 3c. A zero effective stress state is finally reached.

Note, that in contrast to experimental observations, many conventional (elastoplastic or hypoplastic) constitutive models predict a pore pressure accumulation that stops before reaching full liquefaction. This is due to the balancing of positive and negative dilatancy after a certain number of cycles. Such problem is not encountered when using a properly defined HCA model, because only the cumulative trends are described by the constitutive equations. As demonstrated above, in calculations with the HCA model the fully liquefied state ($p^{\text{av}} = q^{\text{av}} = 0$) can be reached.

3 FL and PTL as reference lines from undrained monotonic tests

Beside the ZVADL discussed above, the stress attractors observed in the undrained cyclic tests will be compared also with the failure (FL) and phase transformation lines (PTL) derived from undrained monotonic triaxial tests on the fine sand. These tests were performed with different initial pressures and densities. Both, triaxial compression and extension tests have been conducted. The measured effective stress paths are given in the p - q plane in Figure 4.

The inclinations $M_{c,FL}$ and $M_{e,FL}$ of the failure lines in triaxial compression and extension and the obliquities $M_{c,PTL}$ and $M_{e,PTL}$ of the phase transformation lines derived from the data in Figure 4 have been plotted versus relative density in Figure 5. Obviously, these quantities are density-dependent, which can be described by:

$$M_{c,FL} = 1.41 + 0.21(I_{D0})^{4.2} \quad (20)$$

$$M_{e,FL} = -0.95 - 0.041(I_{D0})^{4.2} \quad (21)$$

$$M_{c,PTL} = 1.03 + 0.65(1 - I_{D0})^{2.4} \quad (22)$$

$$M_{e,PTL} = -0.79 - 0.27(1 - I_{D0})^{1.9} \quad (23)$$

(see the solid or dashed curves in Figure 5, respectively).

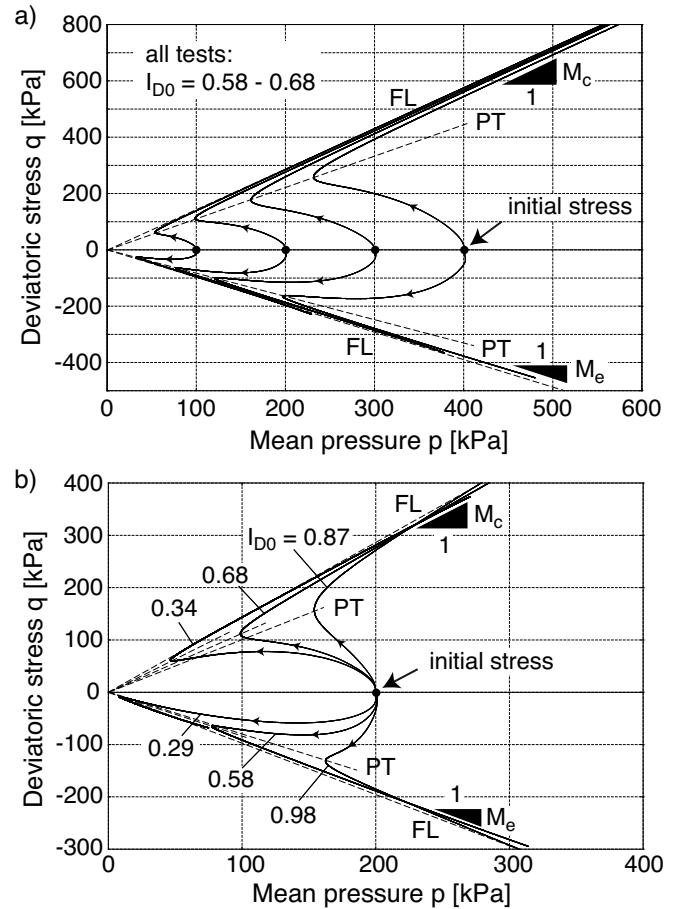


Fig. 4: Effective stress paths in undrained monotonic tests with different a) initial pressures and b) relative densities

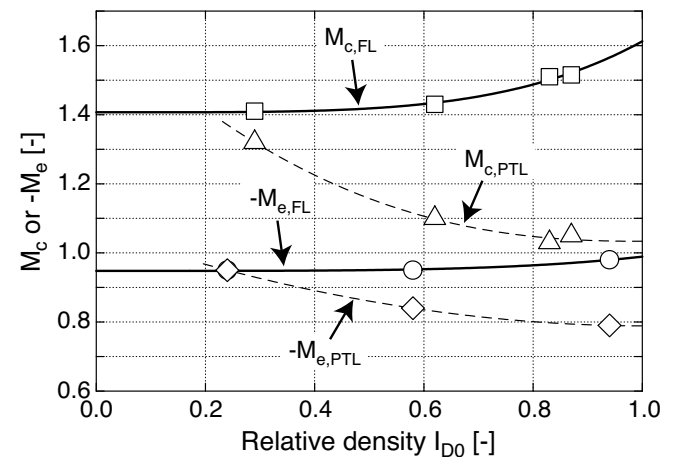


Fig. 5: Inclination M_c or M_e of the failure lines (FL) and the phase transformation lines (PTL) in triaxial compression or extension, respectively, as a function of relative density I_{D0}

The direction of accumulation (cyclic flow rule) has been found rather independent of relative density, stress or strain

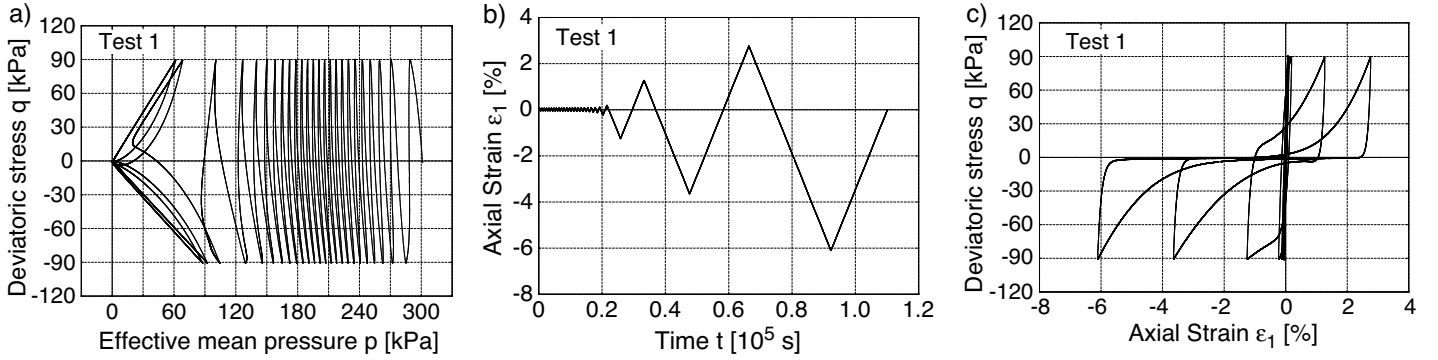


Fig. 6: Results of an undrained cyclic test with isotropic initial stresses and stress cycles ($I_{D0} = 0.63$, $p_0 = 300$ kPa, $\eta_0 = 0$, $q^{\text{ampl}} = 90$ kPa, test No. 1 in Table 1): a) Effective stress path in the p - q -plane, b) Axial strain ε_1 versus time, c) q - ε_1 -hystereses

amplitude and average mean pressure [37–39, 42]. Therefore, in contrast to FL and PTL, the ZVADL is density-independent.

4 Tests with relaxation towards zero effective stress

These tests have been already presented in [41]. In that study, the results have been used to calibrate the bulk modulus K and Poisson's ratio ν of the HCA model stiffness. These tests confirm the stress relaxation paths predicted by the HCA model for the special cases of an isotropic consolidation and stress cycles (case "1" in Figure 3a,b) or an anisotropic consolidation and strain cycles (Figure 3c,d). Therefore, the results are briefly recapitulated in this Section.

4.1 Tests with isotropic consolidation and stress cycles

Several tests with different values of relative density, initial mean pressure and stress amplitude have been performed. Figure 6 shows typical test results for a medium dense sample ($I_{D0} = 0.63$) consolidated at $p_0 = 300$ kPa, $\eta_0 = 0$ and subjected to cycles with an amplitude $q^{\text{ampl}} = 90$ kPa. The test conditions are also summarized in Table 1 (test No. 1). When the effective stress path comes close to the failure line in the triaxial extension regime, it starts to follow a butterfly-shaped loop (Figure 6a) and the axial strain amplitude increases with each subsequent cycle (Figure 6b). Such behaviour is denoted as "cyclic mobility". After the initial liquefaction (i.e. $p = 0$ is reached for the first time) large axial strains appear without mobilizing any significant shear resistance (i.e. $q \approx 0$, Figure 6c). The sample is said to have failed if the axial strain amplitude exceeds a predefined value (e.g. $\varepsilon_1^{\text{ampl}} = 5$ % has been chosen in the present study for the medium dense sand). After initial liquefaction, the average effective stress, i.e. the effective stress at the end of each cycle is zero. Therefore, the test data in Figure 6a confirms the stress attractor $p = q = 0$ predicted by the HCA model for a test with isotropic consolidation and stress cycles (case "1" in Figure 3a,b). Similar conclusions can be drawn from tests on medium dense samples consolidated at other initial pressures (e.g. $p_0 = 100$ kPa in Figure 7a) and from tests on loose ($I_{D0} = 0.24$, Figure 7b) or dense samples ($I_{D0} = 0.82$, Figure 7c), respectively (test Nos. 2-4 in Table 1). The data in Figures 6 and 7 agrees well with numerous experimental studies on

Test No.	I_{D0} [-]	p_0 [kPa]	q_0 [kPa]	η_0 [-]	q^{ampl} [kPa]	$\varepsilon_1^{\text{ampl}}$ [-]
1	0.63	300	0	0	90	-
2	0.61	100	0	0	30	-
3	0.24	300	0	0	45	-
4	0.82	300	0	0	90	-
5	0.66	200	230	1.15	-	6×10^{-4}
6	0.67	200	-4	-0.02	-	6×10^{-4}
7	0.58	200	-148	-0.74	-	6×10^{-4}
8	0.63	300	150	0.50	60	-
9	0.61	300	150	0.50	90	-
10	0.63	300	150	0.50	120	-
11	0.59	200	150	0.75	40	-
12	0.66	200	150	0.75	50	-
13	0.59	200	150	0.75	60	-
14	0.63	150	150	1.00	20	-
15	0.59	150	150	1.00	40	-
16	0.38	300	150	0.50	120	-
17	0.86	300	150	0.50	120	-
18	0.40	200	150	0.75	60	-
19	0.80	200	150	0.75	60	-
20	0.53	50	37.5	0.75	12.5	-
21	0.57	100	75	0.75	25	-
22	0.63	300	225	0.75	75	-
23	0.56	200	200	1.00	60	-
24	0.57	200	100	0.50	60	-
25	0.66	200	60	0.30	60	-
26	0.56	200	50	0.25	60	-
27	0.61	200	-50	-0.25	60	-
28	0.61	200	-50	-0.25	40	-
29	0.66	200	-100	-0.50	40	-

Table 1: Program of undrained cyclic triaxial tests

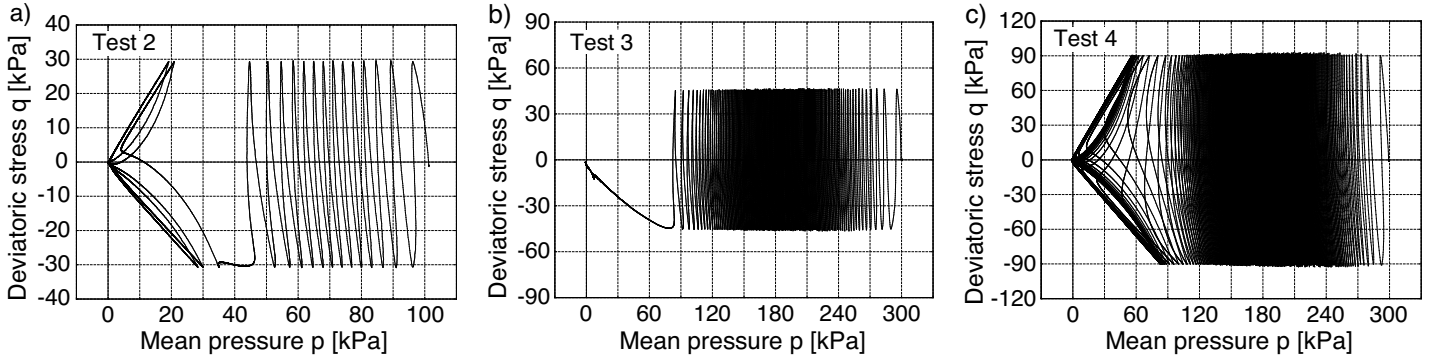


Fig. 7: Effective stress paths from undrained cyclic tests with isotropic initial stresses and stress cycles: a) $I_{D0} = 0.61$, $p_0 = 100$ kPa, $q^{\text{ampl}} = 30$ kPa, b) $I_{D0} = 0.24$, $p_0 = 300$ kPa, $q^{\text{ampl}} = 45$ kPa, c) $I_{D0} = 0.82$, $p_0 = 300$ kPa, $q^{\text{ampl}} = 90$ kPa (test Nos. 2-4 in Table 1)

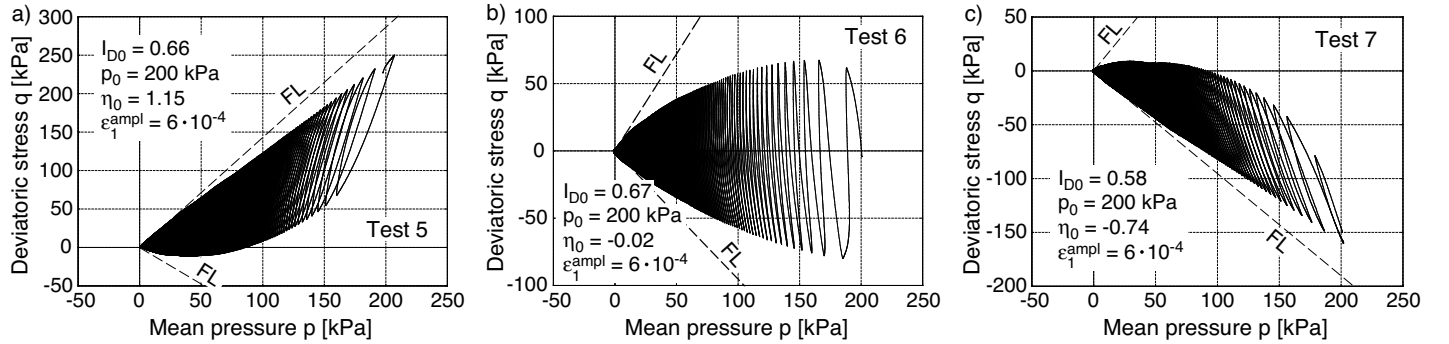


Fig. 8: Effective stress paths in undrained cyclic tests with strain cycles applied on samples consolidated at different η_0 values (all tests: $p_0 = 200$ kPa, $\epsilon_1^{\text{ampl}} = 6 \times 10^{-4}$, $0.58 \leq I_{D0} \leq 0.67$, test Nos. 5-7 in Table 1).

the liquefaction resistance of non-cohesive soils published in the literature. Similar effective stress paths from triaxial, torsional shear or simple shear tests have been presented e.g. in [5, 7–13, 19–21, 24, 25, 29, 32–36, 43, 46–51, 53, 54].

4.2 Tests with strain cycles

The results of three stress relaxation experiments with fully prevented strain accumulation are shown in Figure 8. These effective stress paths have been measured for initial stress ratios $\eta_0 = 1.15$, ≈ 0 and -0.74 (test Nos. 5-7 in Table 1). All samples were medium dense, the initial pressure was $p_0 = 200$ kPa and the strain amplitude was chosen as $\epsilon_1^{\text{ampl}} = 6 \times 10^{-4}$. This strain amplitude lies at the upper boundary of the strain amplitudes usually measured in the drained cyclic tests performed to calibrate the HCA model (Figure 1). It is approximately in the middle of the range of validity $\epsilon^{\text{ampl}} \leq 10^{-3}$ of the HCA model. Results for smaller strain amplitudes are reported in [41]. In good agreement with the scheme in Figure 3c, the strain cycles lead to a relaxation of both q and p until a state with zero effective stress is reached, i.e. $p = q = 0$. Further strain cycles applied in the liquefied state do not affect this asymptotic effective stress (point attractor). This was observed independent of the initial density, initial stress ratio η_0 , initial mean pressure p_0 and strain amplitude [41]. Effective stress paths from strain-controlled undrained cyclic tests are rarely in the literature. Similar data as those shown in Figure 8 have been documented e.g. in [16, 18, 28].

5 Inspection of the stress attractor ZVADL by means of tests with anisotropic consolidation and stress cycles

In order to check the assumption of the ZVADL as a stress attractor, tests with anisotropic consolidation stresses ($\eta_0 \neq 0$) and stress cycles (cases "2" to "4" in Figure 3a) are necessary. Several such tests have been performed in the present study. The initial density, the consolidation stress (p_0 and η_0) and the stress amplitude have been varied. A typical test result for $I_{D0} = 0.61$, $p_0 = 300$ kPa, $\eta_0 = 0.5$ and $q^{\text{ampl}} = 90$ kPa is shown in Figure 9 (test No. 9 in Table 1). After a certain number of cycles the accumulated pore water pressure (i.e. the value at the end of each cycle) reaches an asymptotic value (Figure 9a) and thus the effective stress path stagnates (Figure 9b). Afterwards it repeatedly passes through the same lens-shaped loop in the p - q -plane. The rate of permanent axial strain accumulation decreases with increasing number of cycles (Figure 9c). However, the strain accumulation continues even when the stress relaxation has stopped. The amplitude of axial strain remains almost constant throughout the test (Figure 9c).

In the tests of the present study the cyclic loading was stopped when the accumulated pore water pressure obviously had become stable. At least 1,000 cycles were applied to each sample, unless the failure criterion $|\epsilon_1| = 10\%$ was fulfilled earlier. Since a few of these tests have been also used to inspect the η_0 -dependence of the HCA model stiffness [41], a single drained cycle with the same stress ampli-

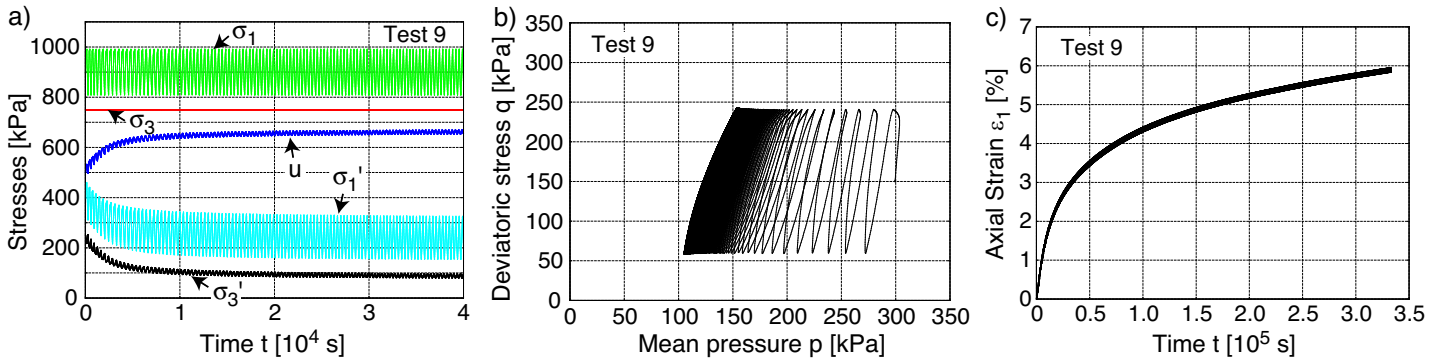


Fig. 9: Results of an undrained cyclic test with anisotropic initial stresses and stress cycles ($p_0 = 300$ kPa, $\eta_0 = 0.5$, $q^{\text{amp}} = 90$ kPa, $I_{D0} = 0.61$, test No. 9 in Table 1): a) Stress components versus time, b) Effective stress path in the p - q -plane, c) Axial strain ε_1 versus time

tude was applied prior to the undrained cyclic loading in all tests. It is advantageous for the analysis of K (for details it is referred to [41]). However, this drained cycle should not affect the stress attractors reached after a sufficiently large number of cycles under undrained conditions.

In the following the position of the final (also termed asymptotic) effective stress loop in the p - q -plane, i.e. the stress loop repeatedly passed through after the accumulated pore water pressure has become stable, is analyzed in comparison to the FL, PTL and ZVADL for various test conditions. In contrast to the FL and the PTL, the inclination $M_{e,ZVADL} = -0.88$ of the ZVADL in the triaxial extension regime has not been determined experimentally, but estimated using $\varphi_{cc} = 31.1^\circ$ calibrated from the drained cyclic tests with triaxial compression.

5.1 Variation of stress amplitude q^{amp}

Three series of tests have been conducted in order to study the influence of stress amplitude. In the first series medium dense samples were consolidated at $p_0 = 300$ kPa, $\eta_0 = 0.5$ and then subjected to an undrained cyclic loading with stress amplitudes $q^{\text{amp}} = 60, 90$ or 120 kPa, respectively (test Nos. 8-10 in Table 1). Figure 10a reveals that an almost constant accumulated pore water pressure is reached in all three tests after a certain number of cycles. The asymptotic pore water pressure increases with increasing stress amplitude. The accumulation of axial strain $\varepsilon_1^{\text{acc}}$ continues even when u^{acc} has become stable (Figure 10b). The effective stress paths are given in Figure 11. The stress loop during the last cycle is highlighted by black colour, while the rest of the stress path is shown in gray. For orientation, the failure line (FL) and the phase transformation line (PTL) with inclinations calculated from Eqs. (20) and (22) for the density of the respective test have been added in Figure 11, together with the ZVADL where zero volumetric strain accumulation was observed in the drained cyclic tests. The ZVADL in Figure 11 has been plotted with $M_{cc} = 1.25$ derived from Figure 1. The asymptotic stress loops for the three different amplitudes are also summarized in Figure 10c. The FL and PTL in Figure 10c have been plotted for an average density $I_{D0} = 0.62$ of the test series. The asymptotic effective stress paths measured in the tests with $q^{\text{amp}} = 90$ and 120 kPa surpass the failure line (Figure 11 and Figure 10c) while the maximum stress of the test with $q^{\text{amp}} = 60$ kPa stays below. The hysteresis of the asymptotic effective stress path increases with increasing

amplitude. The asymptotic average effective stress, i.e. the effective stress at the beginning or end of the last cycle, respectively, is marked by a black circle in Figure 11. It lies near the PTL for the smallest tested amplitude ($q^{\text{amp}} = 60$ kPa), close to the ZVADL for the middle one ($q^{\text{amp}} = 90$ kPa) and between ZVADL and FL for the largest cycles ($q^{\text{amp}} = 120$ kPa), i.e. the larger the amplitude the lower is the asymptotic p^{av} value.

In a second series of tests on medium dense samples the undrained cyclic loading was commenced at a lower pressure $p_0 = 200$ kPa and a higher stress ratio $\eta_0 = 0.75$. Amplitudes of $q^{\text{amp}} = 40, 50$ and 60 kPa were applied (test Nos. 11-13 in Table 1). The effective stress paths are shown in Figure 12. The asymptotic effective stress paths for all three amplitudes remain below the failure line (see also the summary in Figure 13a). The lower the amplitude, the larger is the distance between the maximum deviatoric stress and the failure line. The average effective stress is almost the same for the three tested amplitudes, lying between the PTL and the ZVADL.

Similar conclusions can be drawn from the third test series, where two medium dense samples were consolidated at $p_0 = 150$ kPa and $\eta_0 = 1.00$. Stress amplitudes $q^{\text{amp}} = 20$ and 40 kPa were tested (test Nos. 14-15 in Table 1), leading to the data provided in Figures 14 and 13b. Nearly 3000 cycles had to be applied in the test with $q^{\text{amp}} = 20$ kPa in order to reach a stable value of the accumulated pore water pressure. For the lower amplitude $q^{\text{amp}} = 20$ kPa the maximum deviatoric stress during the asymptotic stress loop lies significantly below the failure line (Figures 14 and 13b). Similar to the data in Figure 13a, the asymptotic average stress observed in the third test series on the influence of amplitude was also located between the PTL and the ZVADL.

5.2 Variation of relative density I_{D0}

The influence of density on the asymptotic effective stress path has been studied in two test series. In the first series three samples with $I_{D0} = 0.38, 0.63$ and 0.86 were consolidated at $p_0 = 300$ kPa, $\eta_0 = 0.50$ and then subjected to an undrained cyclic loading with a relatively large stress amplitude $q^{\text{amp}} = 120$ kPa, corresponding to an amplitude-pressure-ratio of $\zeta = q^{\text{amp}}/p_0 = 0.4$ (test Nos. 16, 10 and 17 in Table 1). The effective stress paths are shown in Figure 15 while the asymptotic stress loops are summarized in Figure 13c. The results for the test No. 10 with $I_{D0} = 0.63$

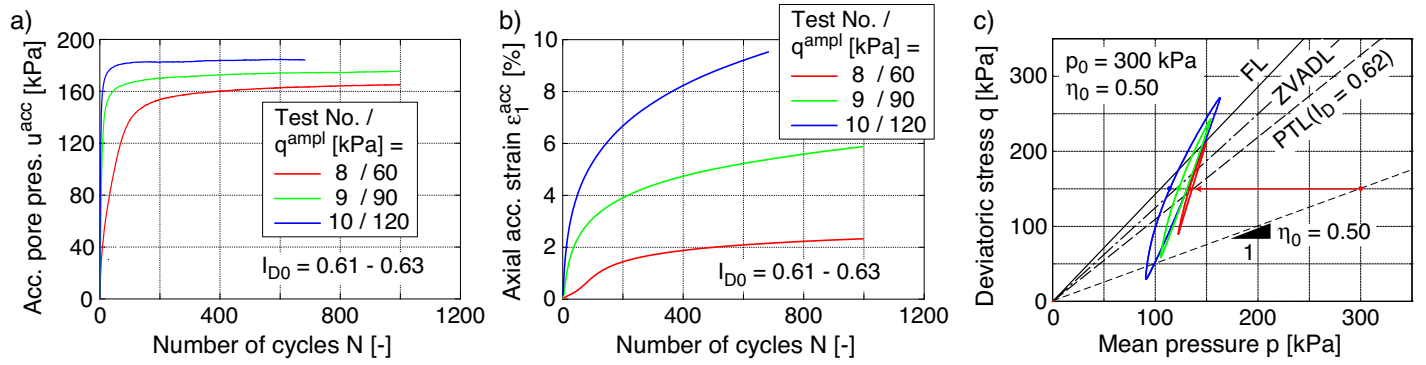


Fig. 10: a) Accumulated pore water pressure $u^{acc}(N)$, b) accumulated axial strain $\epsilon_1^{acc}(N)$ and c) effective stress path during the last cycle in three tests with different stress amplitudes (test Nos. 8-10 in Table 1)

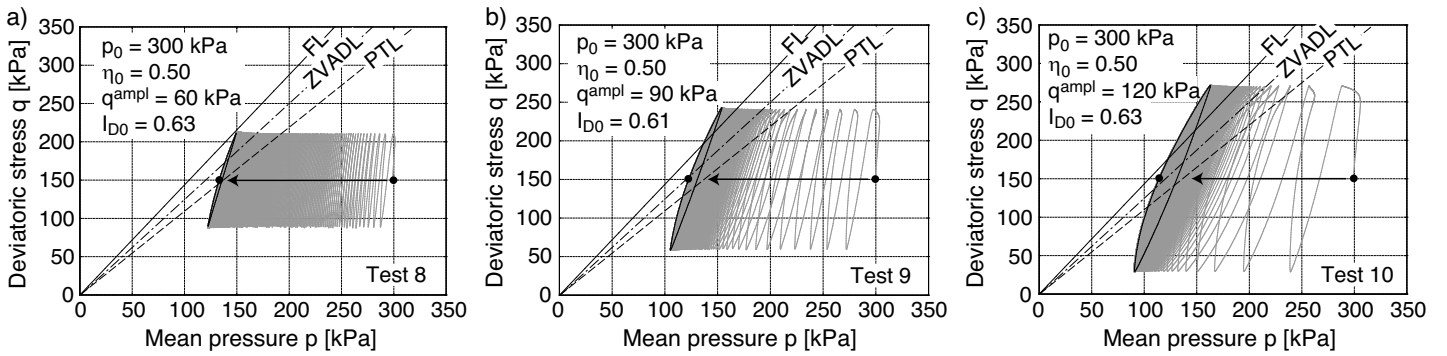


Fig. 11: Effective stress paths measured in undrained cyclic tests with anisotropic consolidation stresses and different stress amplitudes $q^{ampl} = 60, 90$ and 120 kPa (all tests: $p_0 = 300$ kPa, $\eta_0 = 0.50$, $0.61 \leq I_{D0} \leq 0.63$, test Nos. 8-10 in Table 1)

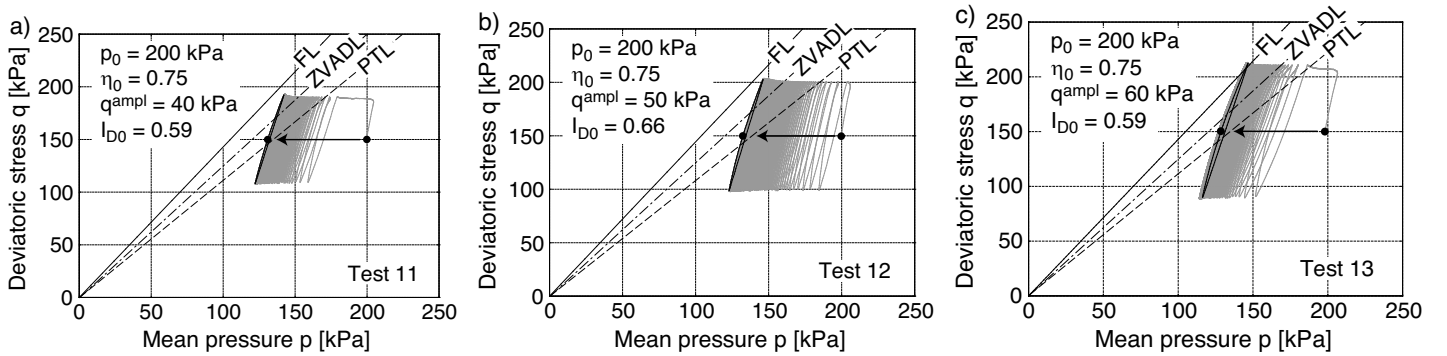


Fig. 12: Effective stress paths measured in undrained cyclic tests with anisotropic consolidation stresses and different stress amplitudes $q^{ampl} = 40, 50$ and 60 kPa (all tests: $p_0 = 200$ kPa, $\eta_0 = 0.75$, $0.59 \leq I_{D0} \leq 0.66$, test Nos. 11-13 in Table 1)

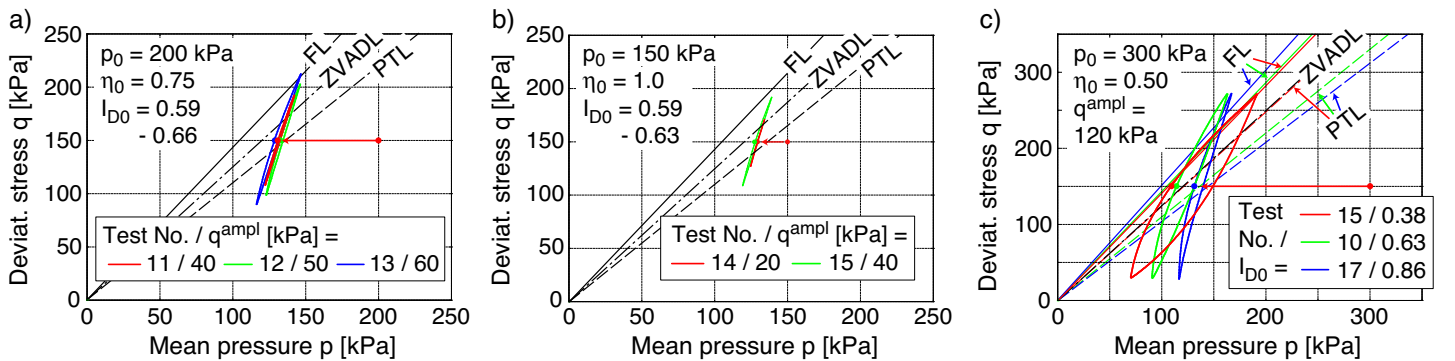


Fig. 13: Effective stress paths during the last cycle in tests with different a), b) amplitudes and c) densities

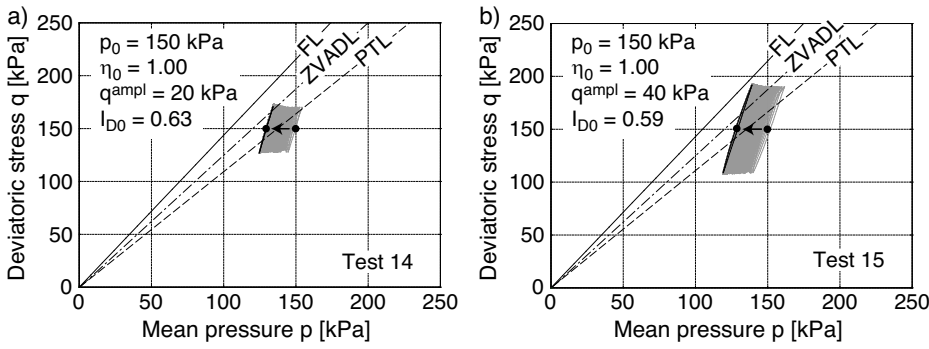


Fig. 14: Effective stress paths measured in undrained cyclic tests with anisotropic consolidation stresses and different stress amplitudes $q^{\text{amp}} = 20$ and 40 kPa (all tests: $p_0 = 150$ kPa, $\eta_0 = 1.00$, $0.59 \leq I_{D0} \leq 0.63$, test Nos. 14-15 in Table 1)

(Figure 15b) have been already shown in Figure 11c. They are repeated here for comparison purpose. The diagrams in Figure 15 reveal that the area enclosed by the asymptotic stress loop increases with decreasing density while its inclination decreases. The stress path during the last cycle measured for the loosest sample adapts to the failure line, while the maximum deviatoric stress goes beyond the failure line in the case of the medium dense and dense sample. The asymptotic average stress lies close to the FL in case of the loose sample, slightly above the ZVADL for the medium dense sample and between PTL and ZVADL for the dense sand. Therefore, the asymptotic p^{av} value increases with increasing density.

In a second test series samples with initial densities of $I_{D0} = 0.40, 0.59$ and 0.80 have been consolidated at $p_0 = 200$ kPa and $\eta_0 = 0.75$. The undrained cyclic loading was applied with a stress amplitude of $q^{\text{amp}} = 60$ kPa, i.e. $\zeta = 0.3$ (test Nos. 18, 13 and 19 in Table 1). The effective stress paths are provided in Figure 16. The results for the test with $I_{D0} = 0.59$ (Figure 16b) have been already shown in Figure 12c. The stress loops passed through during the last cycle are summarized in Figure 17a. With increasing density, the asymptotic stress loop is shifted to the right in the p - q -plane. In the test on the loose sample the effective stress path during the last cycles slightly surpassed the failure line, while in case of the dense sample the maximum deviatoric stress was far below the FL. The asymptotic average stresses lay near the ZVADL for $I_{D0} = 0.40$, between ZVADL and PTL for $I_{D0} = 0.59$ and near the PTL for $I_{D0} = 0.80$. The tendency of increasing asymptotic p^{av} with increasing density agrees well with the first test series.

5.3 Variation of initial mean pressure p_0

Four medium dense samples ($0.53 \leq I_{D0} \leq 0.66$) were consolidated at different pressures $p_0 = 50, 100, 200$ and 300 kPa. The initial stress ratio $\eta_0 = 0.75$ and the amplitude-pressure-ratio $\zeta = 0.25$ were the same in all tests (test Nos. 12 and 20-22 in Table 1). The effective stress paths measured in the tests with $p_0 = 50, 100$ and 300 kPa are given in Figure 18. The results of the test No. 12 with $p_0 = 200$ kPa have been already provided in the Figure 12b. The effective stress paths during the last cycles of the four tests are also collected in Figure 17b. In these tests the stress relaxation stopped when the maximum stress during a cycle touched the failure line. The average effective stress during the last cycles lies somewhere between the PTL and the ZVADL in all four tests.

Two medium dense samples consolidated at the same initial deviatoric stress $q_0 = 150$ kPa but at different initial mean pressures $p_0 = 200$ or 300 kPa, respectively, can be also compared. The stress amplitude $q^{\text{amp}} = 60$ kPa was the same in both tests (test Nos. 8 and 13 in Table 1). The effective stress paths are given in Figure 11a and in Figure 12c. The asymptotic stress loops compared in Figure 17c are nearly identical. Similar data for two other samples are provided in Figure 19a. These samples were consolidated at either $p_0 = 150$ or 200 kPa, respectively, keeping $q_0 = 150$ kPa and $q^{\text{amp}} = 40$ kPa constant (test Nos. 11 and 15 in Table 1). The effective stress path of the test No. 11 with $p_0 = 200$ kPa is given in Figure 12a, that of test No. 15 with $p_0 = 150$ kPa is provided in Figure 14b. Looking at the asymptotic stress loops in Figures 17c and 19a, for a constant stress amplitude the consolidation pressure p_0 seems to be of secondary importance.

5.4 Variation of initial stress ratio η_0

The influence of initial stress ratio η_0 can be judged by five tests with samples consolidated at $p_0 = 200$ kPa and different stress ratios $\eta_0 = 0.25, 0.30, 0.5, 0.75$ and 1.0 in the triaxial compression regime. All samples were medium dense and subjected to an undrained cyclic loading with $q^{\text{amp}} = 60$ kPa (test Nos. 13 and 23-26 in Table 1). The effective stress paths for the tests Nos. 24-26 with $\eta_0 = 0.25, 0.30$ and 0.5 are provided in Figure 20. The test No. 13 with $\eta_0 = 0.75$ has been already shown in Figure 12c. The asymptotic stress loops are collected in Figure 19b. As obvious from Figure 20, the shape of the effective stress path during the final stage of a test depends strongly on the initial stress ratio and on whether the stress path enters the extension regime or not. In case that $q_{\text{min}} \geq 0$ lens-shaped asymptotic stress loops are obtained which show a larger hysteresis with decreasing initial stress ratio η_0 . In contrast, in the test with $\eta_0 = 0.25$, where the minimum deviatoric stress lies below the p -axis, the effective stress path during the last cycles shows a butterfly-like shape. It adapts to the failure lines in the compression and extension regime of the p - q -plane. While the maximum deviatoric stress during the last cycles surpasses the FL in case of the tests with $\eta_0 = 0.3$ and 0.5 , it is located almost on the FL for $\eta_0 = 0.75$ and 1.0 . The effective stress at the end of the last cycle lies near the FL in case of the tests with $\eta_0 = 0.25$ and 0.30 , close to the ZVADL for $\eta_0 = 0.50$ and between PTL and ZVADL for the higher tested initial stress ratios.

The ε_1 - t diagrams in Figure 21a,b show that also the

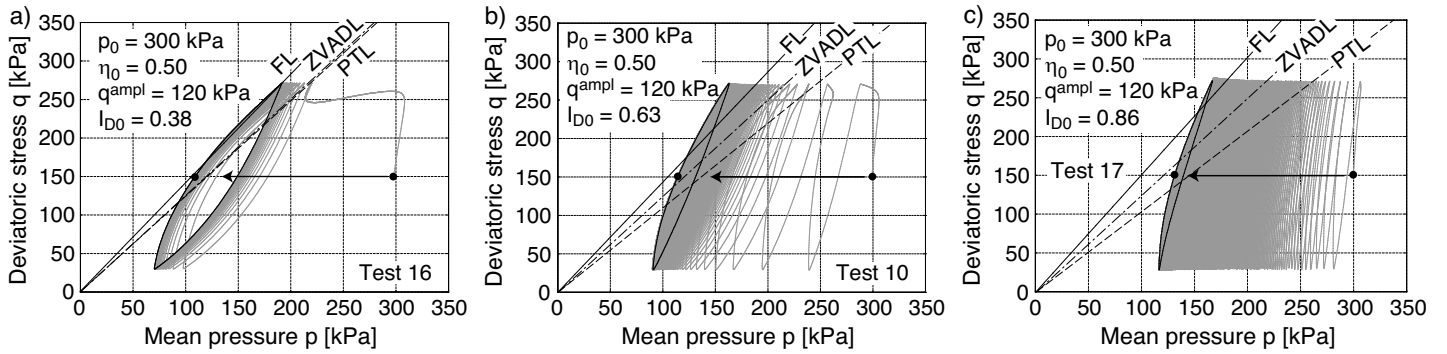


Fig. 15: Effective stress paths measured in undrained cyclic tests with anisotropic consolidation stresses and different initial relative densities $I_{D0} = 0.38, 0.63$ and 0.86 (all tests: $p_0 = 300$ kPa, $\eta_0 = 0.50$, $q^{amp} = 120$ kPa, test Nos. 16, 10 and 17 in Table 1)

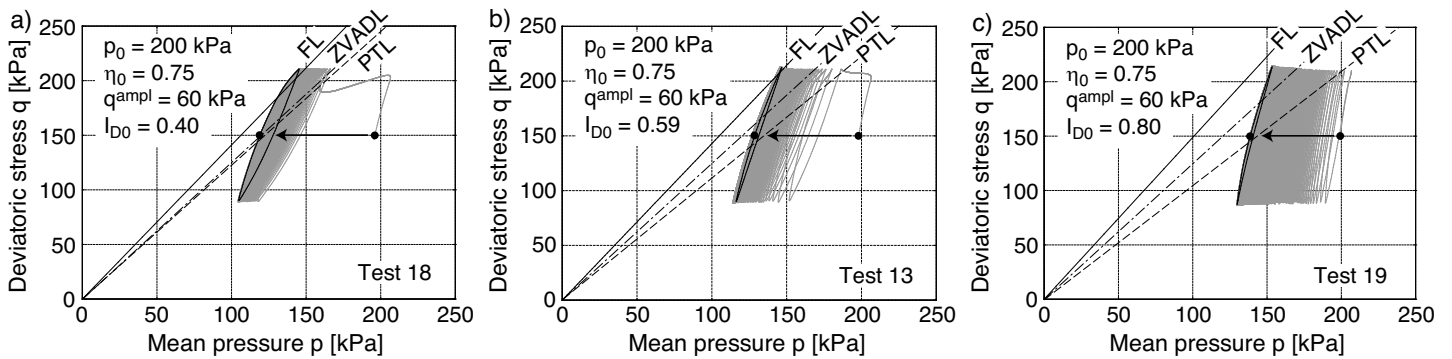


Fig. 16: Effective stress paths measured in undrained cyclic tests with anisotropic consolidation stresses and different initial relative densities $I_{D0} = 0.40, 0.59$ and 0.80 (all tests: $p_0 = 200$ kPa, $\eta_0 = 0.75$, $q^{amp} = 60$ kPa, test Nos. 18, 13 and 19 in Table 1)

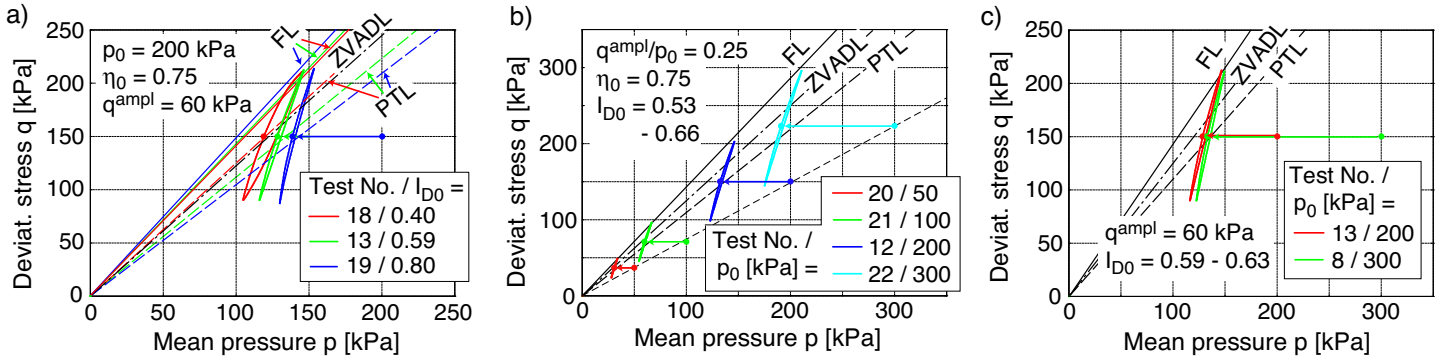


Fig. 17: Effective stress paths during the last cycle in tests with different a) initial relative densities b) initial pressures p_0 at $\eta_0 =$ constant and c) initial pressures p_0 at $q_0 =$ constant

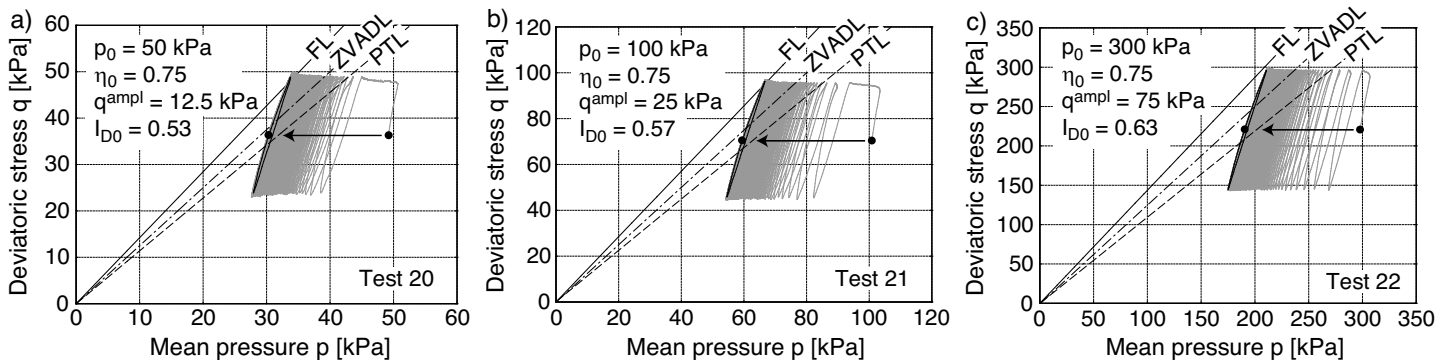


Fig. 18: Effective stress paths measured in undrained cyclic tests with anisotropic consolidation at different pressures $p_0 = 50, 200$ and 300 kPa (all tests: $\eta_0 = 0.75$, $\zeta = q^{amp}/p_0 = 0.25, 0.53 \leq I_{D0} \leq 0.66$, test Nos. 20-22 in Table 1)

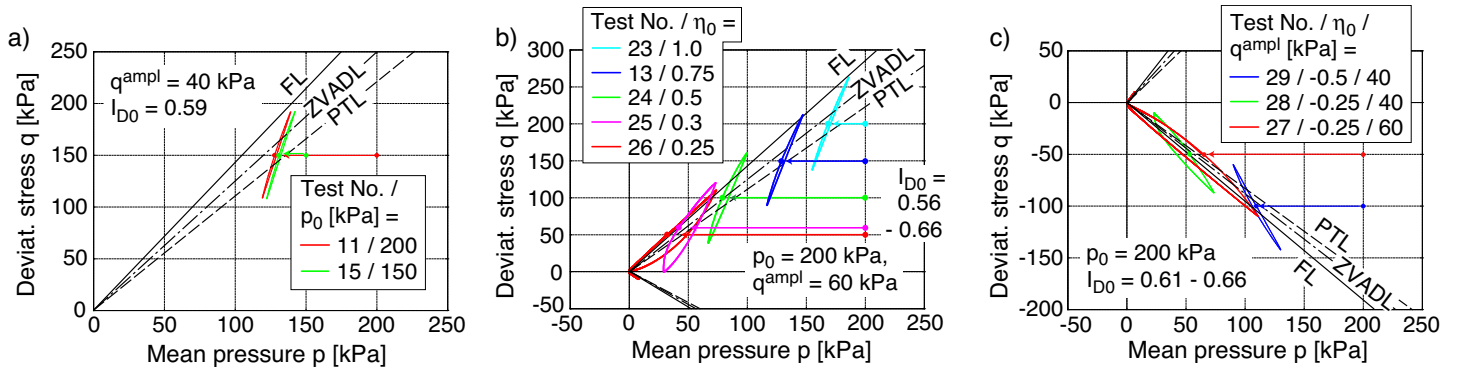


Fig. 19: Effective stress paths during the last cycle in tests with different a) initial pressures p_0 at $q_0 = \text{constant}$ and b),c) initial stress ratios η_0 at $p_0 = \text{constant}$

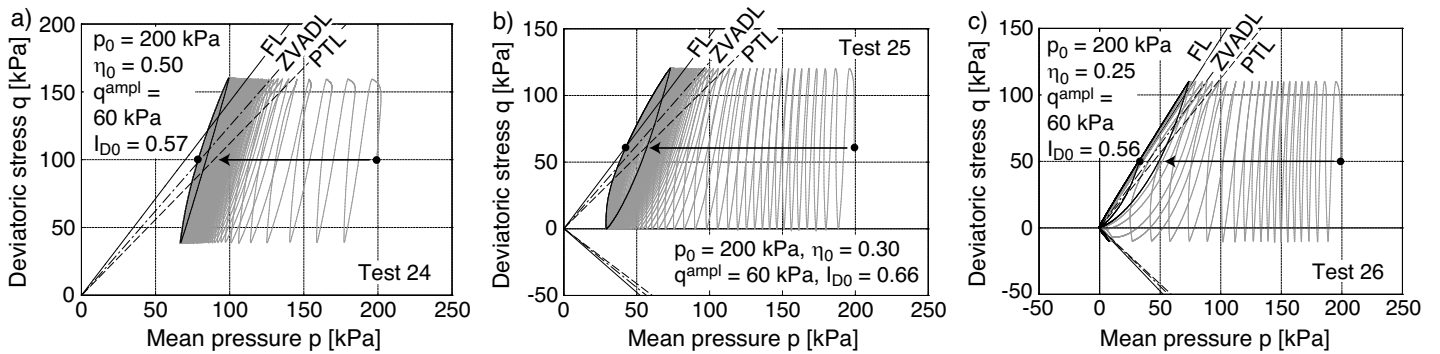


Fig. 20: Effective stress paths measured in undrained cyclic tests with anisotropic consolidation stresses and different initial stress ratios $\eta_0 = 0.50, 0.30$ and 0.25 (all tests: $p_0 = 200$ kPa, $q^{\text{ampl}} = 60$ kPa, $0.56 \leq I_{D0} \leq 0.66$, test Nos. 24-26 in Table 1)

development of axial strain with time is totally different in the tests Nos. 25 and 26 with only slightly different η_0 values. In the test with $\eta_0 = 0.30$ and $q_{\text{min}} = 0$ a pronounced accumulation of axial strain is observed while the strain amplitude remains relatively small (similar to Figure 9c). In the case of the test with $\eta_0 = 0.25$ and $q_{\text{min}} < 0$ the strain amplitude significantly increases after initial liquefaction, i.e. the curves $\varepsilon_1(t)$ are similar to the tests with isotropic consolidation ($\eta_0 = 0$, see Figure 6b).

A similar test series on medium dense samples has been performed in the triaxial extension regime. All tests were started at $p_0 = 200$ kPa and either $\eta_0 = -0.25$ or -0.5 . Two different stress amplitudes $q^{\text{ampl}} = 40$ and 60 kPa have been applied (test Nos. 27-29 in Table 1). The test results are shown in Figures 22 and 19c. The inclination of the average effective stress paths is opposite to that observed in the triaxial compression tests (compare Figures 20 and 22). In the test with $\eta_0 = -0.25$ and $q^{\text{ampl}} = 60$ kPa the maximum deviatoric stress surpassed the isotropic axis, i.e. $q^{\text{max}} > 0$. In the final stage of this test the effective stress path (Figure 22a) was butterfly-shaped, adapting to the failure lines in the triaxial extension and compression regime of the p - q -plane. In the two other tests with $q^{\text{max}} < 0$ the asymptotic stress loop was lens-shaped. In both tests the minimum deviatoric stress during the last cycles went below the failure line. The asymptotic average stress lies on the FL in case of the test with $\eta_0 = -0.25$ and $q^{\text{ampl}} = 40$ kPa, near the PTL for $\eta_0 = -0.25$ and $q^{\text{ampl}} = 60$ kPa and close to the ZVADL for $\eta_0 = -0.5$ and $q^{\text{ampl}} = 40$ kPa. It should be kept in mind, however, that the ZVADL in the triaxial

extension regime has not been determined experimentally for the tested fine sand but estimated from the results of the drained cyclic triaxial compression tests.

The curve $\varepsilon_1(t)$ of test No. 28, i.e. for $q^{\text{max}} < 0$ in Figure 21c shows a pronounced accumulation of extensional axial strain. The development of axial strain with time in test No. 27 with $q^{\text{max}} > 0$ is similar to that measured in test No. 26 (Figure 21b), with the exception that the accumulation of strain during the first cycles goes towards the extension side.

5.5 Comparison with the literature

There is a general consensus in the literature that unsymmetrical stress cycles (i.e. $q^{\text{av}} \neq 0$ and $q^{\text{ampl}} > |q^{\text{av}}|$ in triaxial tests, or $\tau^{\text{av}} \neq 0$ and $\tau^{\text{ampl}} > |\tau^{\text{av}}|$ in torsional or simple shear tests) lead to butterfly-shaped stress paths, temporarily passing a zero effective stress state $p = q = 0$, if the density is sufficiently large (i.e. at least medium dense) [4, 9, 14, 15, 25, 34, 46, 50, 51]. This agrees well with the data shown in Figures 20c and 22a.

For a cyclic loading with $q_{\text{min}} = 0$ (triaxial) or $\tau_{\text{min}} = 0$ (torsional or simple shear) the data in the literature are somewhat ambiguous. When the accumulated pore water pressure had become stable, some researchers found lens-shaped stress paths adapting to the failure line, with $p > 0$ at $q = q_{\text{min}} = 0$ for various densities from loose to dense [2, 9, 29, 34]. Those observations are in accordance with the results in Figure 20b. In other studies on loose to medium dense samples $p \approx 0$ was reached at $q = q_{\text{min}} = 0$ [4, 25, 46]. Hyodo et al. [14] found an influence of density, since $p =$

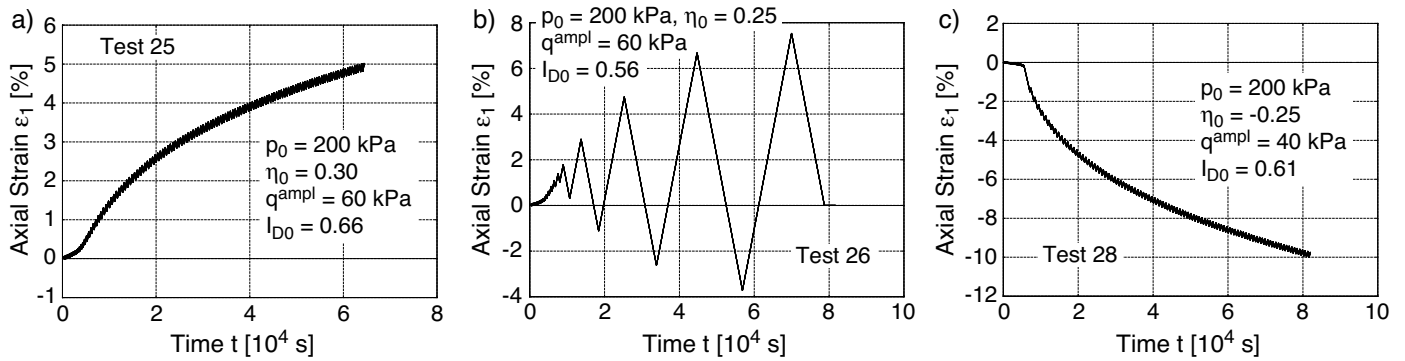


Fig. 21: Development of axial strain ε_1 with time t in tests with different initial stress ratios η_0

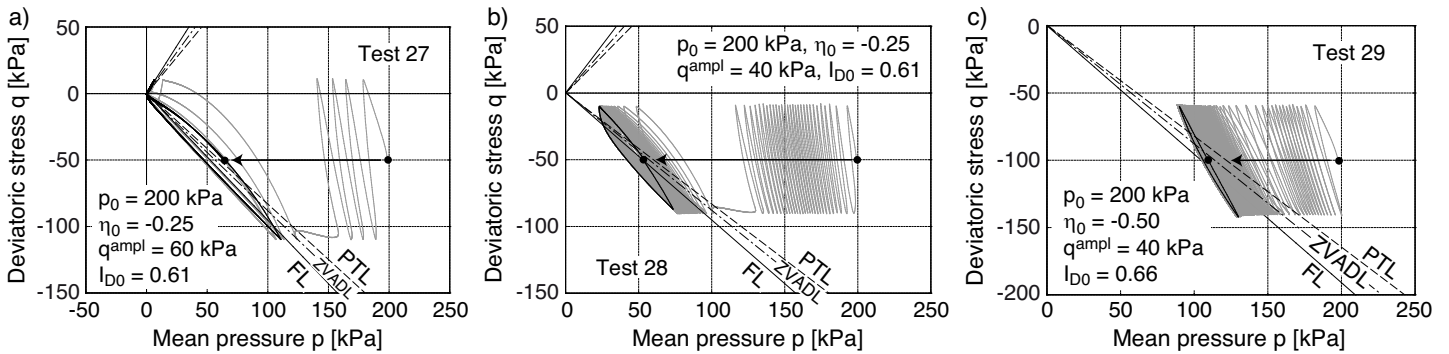


Fig. 22: Effective stress paths measured in undrained cyclic tests with anisotropic consolidation stresses in the triaxial extension regime (all tests: $p_0 = 200$ kPa, $q^{\text{ampl}} = 40$ or 60 kPa, $0.61 \leq I_{D0} \leq 0.66$, test Nos. 27-29 in Table 1)

0 was reached for a loose sample while the effective stress path stopped at $p > 0$ in the case of dense sand. Recently, Sze and Yang [32] observed a dependence on the specimen preparation method: While $p = 0$ at $q = 0$ was reached for air-pluviated samples, the stress relaxation stopped at $p > 0$ for samples prepared by moist tamping. In the present study, however, an asymptotic effective stress loop with $p > 0$ at $q = 0$ was also measured for pluviated samples (Figure 20b). The data from some other test series in the literature with $q_{\min} = 0$ (e.g. [51]) do not allow to judge the location of the asymptotic effective stress path with respect to the FL, because the cyclic loading was stopped before an asymptotic value of accumulated pore water pressure was reached.

Lens-shaped asymptotic stress paths from cyclic tests with $q_{\min} > 0$ or $\tau_{\min} > 0$ have been reported by several researchers [2, 4, 14, 15, 25, 27, 30, 32, 34, 46]. Insofar, the effective stress paths presented in Figures 11, 12, 14, 15, 16, 18 and 20a agree well with the literature. In some tests the effective stress path measured after the accumulated pore water pressure had become stable went beyond the FL known from monotonic tests [4, 14, 27, 30], while q^{\max} was found lying on or below the FL in some other studies [15, 34, 51]. No clear correlation between the location of the asymptotic q^{\max} with respect to the FL and parameters like density, sample preparation technique, initial stress and stress amplitude can be derived from those studies. In torsional shear tests with a K_0 consolidation of the samples and torsional cycles applied with $\tau^{\text{av}} = 0$, the effective stress path of loose samples stopped at the PTL while that of dense ones was bound by the FL [7]. In several publications [2, 25, 32, 46] no direct comparison of the effective

stress path with the FL or PTL has been undertaken. Furthermore, the authors could not find any published effective stress paths from tests with cycles completely lying in the triaxial extension regime of the p - q -plane (similar to the data in Figure 22b,c).

5.6 Summary of asymptotic stress loops

Figure 23 summarizes all measured asymptotic stress loops in the p - q plane. The medium dense samples are marked by the blue loops while the data for loose or dense sand is distinguished by the red or green loops, respectively. Three characteristic points of the asymptotic stress loop, namely its initial point, maximum (triaxial compression) or minimum (triaxial extension) point and center are collected in Figure 24. With the exception of the loops for loose sand and large amplitudes, the initial and the center points of a test lie close to each other. The maxima (compression) or minima (extension) of the stress loops (blue or cyan points) scatter around the failure line (shown for $I_{D0} = 0.6$ in Figure 24). Most initial points (red points) lie close to the ZVAD line derived from the drained cyclic tests.

As explained above, the HCA model predicts a stress relaxation until the average stress reaches the ZVAD line. Looking at Figure 24 this assumption seems approximately justified, although the real material behaviour is more complicated, showing an amplitude and void ratio dependence of the stress attractors.

6 Summary and conclusions

The stress attractors predicted by the high-cycle accumulation (HCA) model of Niemunis et al. [23] have been ex-

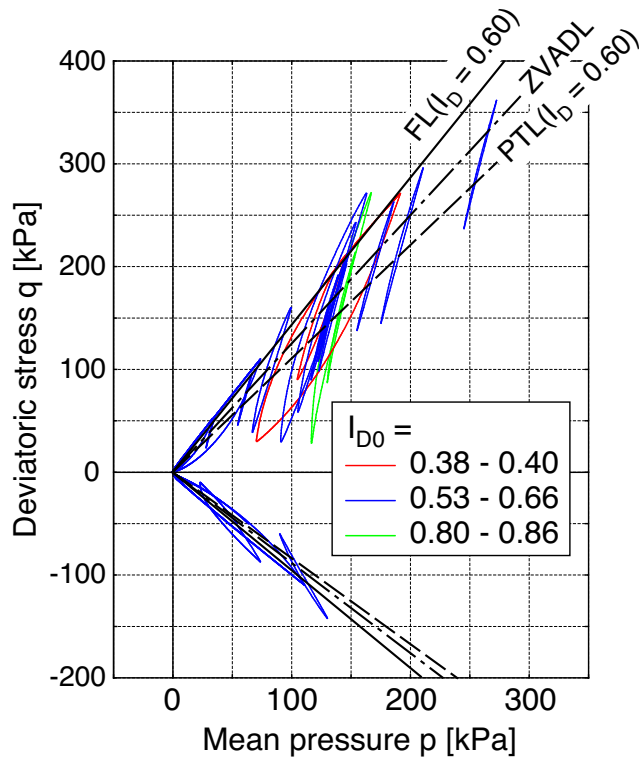


Fig. 23: Summary of asymptotic stress loops in the p - q plane

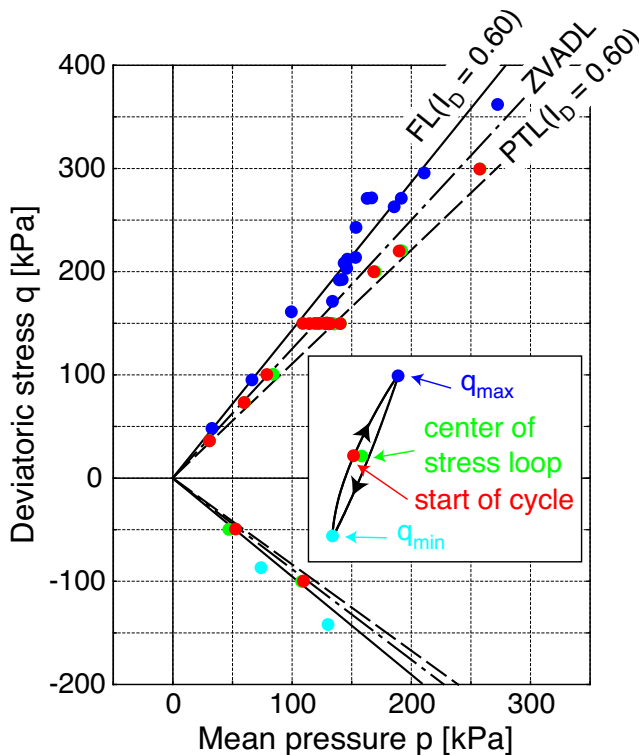


Fig. 24: Summary of characteristic points of the asymptotic stress loops in the p - q plane

amined based on the data from stress relaxation experiments, i.e. undrained cyclic triaxial tests performed on a fine sand. First, the data from an earlier test series [41] with isotropic consolidation and stress cycles or anisotropic consolidation and strain cycles, respectively, are recapitulated. The experimentally observed stress relaxation towards $p^{av} = q^{av} = 0$ full liquefaction is in good agreement with the HCA model prediction.

The present paper concentrates on a new test series with anisotropic consolidation and stress cycles performed on the same fine sand. In these tests the initial density, the initial stress (p_0, η_0) and the stress amplitude q^{amp1} have been varied. The accumulated pore water pressure became stable after a sufficiently large number of cycles and the effective stress path repeatedly passed through the same loop in the p - q plane. For stress paths completely lying in either the triaxial compression ($q_{min} > 0$) or extension regime ($q_{max} < 0$) of the p - q plane, lens-shaped asymptotic stress loops have been measured. The area enclosed by these lenses increases with decreasing values of density and initial stress ratio and with increasing stress amplitude. In case of low densities or large stress amplitudes, the maximum deviatoric stress during the final stress loop surpassed the failure line (FL) known from undrained monotonic tests. In contrast, for small stress amplitudes it has been found significantly below the FL. If unsymmetrical stress cycles were applied around the p -axis, i.e. with $q^{av} \neq 0$ and $q^{amp1} > |q^{av}|$, the effective stress path during the last cycles showed a butterfly-like shape.

The HCA model predicts a relaxation of the average effective stress until a stress ratio $\eta^{av} = q^{av}/p^{av} = M$ ($M = M_{cc}$ for triaxial compression, $M = M_{ec}$ for extension) is reached. Usually, M is calibrated from drained cyclic triaxial tests with different average stress ratios. M corresponds to the stress ratio with zero volumetric strain accumulation. It is similar to the critical stress ratio derived from monotonic shear tests. The corresponding line in the p - q -plane inclined by M is denoted as ZVADL (zero volumetric accumulation drained) herein. The asymptotic average stress ratios observed in the present tests after the accumulated pore water pressure had become stable, lie close to the ZVADL. Insofar, the stress attractors incorporated into the HCA model could be approximately confirmed by the present test series.

Acknowledgement

This research has been performed in the framework of the project "Improvement of an accumulation model for high-cyclic loading" (TR 218/18-1). The authors are grateful to DFG (German Research Council) for the financial support.

References

- [1] M. Abdelkrim, P. De Buhan, and G. Bonnet. A general method for calculating the traffic load-induced residual settlement of a platform, based on a structural analysis approach. *Soils and Foundations*, 46(4):401-414, 2006.
- [2] G. Arangelovski and I. Towhata. Accumulated deformation of sand with initial shear stress and effective stress state lying near failure conditions. *Soils and Foundations*, 44(6):1-16, 2004.
- [3] C.S. Chang and R.V. Whitman. Drained permanent deformation of sand due to cyclic loading. *Journal of Geotechnical Engineering, ASCE*, 114(10):1164-1180, 1988.

- [4] G. Chiaro, J. Koseki, and T. Sato. Effects of initial static shear on liquefaction and large deformation properties of loose saturated Toyoura sand in undrained cyclic torsional shear tests. *Soils and Foundations*, 52(3):498–510, 2012.
- [5] H.K. Dash, T.G. Sitharam, and B.A. Baudet. Influence of non-plastic fines on the response of a silty sand to cyclic loading. *Soils and Foundations*, 50(5):695–704, 2010.
- [6] R. Galindo, M. Illueca, and R. Jimenez. Permanent deformation estimates of dynamic equipment foundations: Application to a gas turbine in granular soils. *Soil Dynamics and Earthquake Engineering*, 63:8–18, 2014.
- [7] V.N. Georgiannou and M. Konstadinou. Effects of density on cyclic behaviour of anisotropically consolidated Ottawa sand under undrained torsional loading. *Géotechnique*, 64(4):287–302, 2014.
- [8] V.N. Georgiannou and A. Tsomokos. Comparison of two fine sands under torsional loading. *Canadian Geotechnical Journal*, 45:1659–1672, 2008.
- [9] V.N. Ghionna and D. Porcino. Liquefaction resistance of undisturbed and reconstituted samples of a natural coarse sand from undrained triaxial tests. *Journal of Geotechnical and Geoenvironmental Engineering, ASCE*, 132(2):194–201, 2006.
- [10] M. Hatanaka, L. Feng, N. Matsumura, and H. Yasu. A study on the engineering properties of sand improved by the sand compaction pile method. *Soils and Foundations*, 48(1):73–85, 2008.
- [11] M. Hatanaka, A. Uchida, and J. Ohara. Liquefaction characteristics of a gravelly fill liquefied during the 1995 Hyogo-Ken Nanbu earthquake. *Soils and Foundations*, 37(3):107–115, 1997.
- [12] M. Hyodo, A.F.L. Hyde, and N. Aramaki. Liquefaction of crushable soils. *Géotechnique*, 48(4):527–543, 1998.
- [13] M. Hyodo, A.F.L. Hyde, N. Aramaki, and Y. Nakata. Undrained monotonic and cyclic shear behaviour of sand under low and high confining stresses. *Soils and Foundations*, 42(3):63–76, 2002.
- [14] M. Hyodo, H. Murata, N. Yasufuku, and T. Fujii. Undrained cyclic shear strength and residual shear strain of saturated sand by cyclic triaxial tests. *Soils and Foundations*, 31(3):60–76, 1991.
- [15] M. Hyodo, H. Tanimizu, N. Yasufuku, and H. Murata. Undrained cyclic and monotonic triaxial behaviour of saturated loose sand. *Soils and Foundations*, 34(1):19–32, 1994.
- [16] Y. Jafarian, I. Towhata, M.H. Baziar, A. Noorzad, and A. Bahmanpour. Strain energy based evaluation of liquefaction and residual pore water pressure in sands using cyclic torsional shear experiments. *Soil Dynamics and Earthquake Engineering*, 35:13–28, 2012.
- [17] C. Karg, S. Francois, W. Haegeman, and G. Degrande. Elasto-plastic long-term behavior of granular soils: modeling and experimental validation. *Soil Dynamics and Earthquake Engineering*, 30(8):635–646, 2010.
- [18] M. Kazama, A. Yamaguchi, and E. Yanagisawa. Liquefaction resistance from a ductility viewpoint. *Soils and Foundations*, 40(6):47–60, 2000.
- [19] T. Kiyota, J. Koseki, and T. Sato. Relationship between limiting shear strain and reduction of shear moduli due to liquefaction in large strain torsional shear tests. *Soil Dynamics and Earthquake Engineering*, 49:122–134, 2013.
- [20] T. Kiyota, T. Sato, J. Koseki, and M. Abadimarand. Behavior of liquefied sands under extremely large strain levels in cyclic torsional shear tests. *Soils and Foundations*, 48(5):727–739, 2008.
- [21] M. Konstadinou and V.N. Georgiannou. Cyclic behaviour of loose anisotropically consolidated Ottawa sand under undrained torsional loading. *Géotechnique*, 63(13):1144–1158, 2013.
- [22] M.P. Luong. Mechanical aspects and thermal effects of cohesionless soils under cyclic and transient loading. In *Proc. IUTAM Conf. on Deformation and Failure of Granular materials, Delft*, pages 239–246, 1982.
- [23] A. Niemunis, T. Wichtmann, and T. Triantafyllidis. A high-cycle accumulation model for sand. *Computers and Geotechnics*, 32(4):245–263, 2005.
- [24] M. Oda, K. Kawamoto, K. Suzuki, H. Fujimori, and M. Sato. Microstructural interpretation on reliquefaction of saturated granular soils under cyclic loading. *Journal of Geotechnical and Geoenvironmental Engineering, ASCE*, 127(5):416–423, 2001.
- [25] F. Oka, A. Yashima, A. Tateishi, Y. Taguchi, and S. Yamashita. A cyclic elasto-plastic constitutive model for sand considering a plastic-strain dependence of the shear modulus. *Géotechnique*, 49(5):661–680, 1999.
- [26] C. Pasten, H. Shin, and J.C. Santamarina. Long-Term Foundation Response to Repetitive Loading. *Journal of Geotechnical and Geoenvironmental Engineering, ASCE*, 140(4), 2014.
- [27] D. Porcino, G. Caridi, and V.N. Ghionna. Undrained monotonic and cyclic simple shear behaviour of carbonate sand. *Géotechnique*, 58(8):635–644, 2008.
- [28] K. Sassa, G. Wang, H. Fukuoka, and D.A. Vankov. Shear-Displacement-Amplitude Dependent Pore-Pressure Generation in Undrained Cyclic Loading Ring Shear Tests - An Energy Approach. *Journal of Geotechnical and Geoenvironmental Engineering, ASCE*, 131(6):750–761, 2005.
- [29] S.S. Sharma and M. Ismail. Monotonic and cyclic behavior of two calcareous soils of different origins. *Journal of Geotechnical and Geoenvironmental Engineering, ASCE*, 132(12):1581–1591, 2006.
- [30] S. Sivathayalan and D. Ha. Effect of static shear stress on the cyclic resistance of sands in simple shear loading. *Canadian Geotechnical Journal*, 48:1471–1484, 2011.
- [31] A.S.J. Suiker and R. de Borst. A numerical model for the cyclic deterioration of railway tracks. *International Journal for Numerical Methods in Engineering*, 57:441–470, 2003.
- [32] H.Y. Sze and J. Yang. Failure Modes of Sand in Undrained Cyclic Loading: Impact of Sample Preparation. *Journal of Geotechnical and Geoenvironmental Engineering, ASCE*, 140(1):152–169, 2014.
- [33] F. Tatsuoka, S. Toki, S. Miura, Kato H., M. Okamoto, S.-I. Yamada, S. Yasuda, and F. Tanizawa. Some factors affecting cyclic undrained triaxial strength of sand. *Soils and Foundations*, 26(3):99–116, 1986.
- [34] Y.P. Vaid and J.C. Chern. Effect of static shear on resistance to liquefaction. *Soils and Foundations*, 28(1):47–60, 1983.
- [35] Y.P. Vaid, E.K.F. Chung, and R.H. Kuerbis. Preshearing and undrained response of sands. *Soils and Foundations*, 29(4):49–61, 1989.
- [36] Y.P. Vaid and S. Sivathayalan. Fundamental factors affecting liquefaction susceptibility of sands. *Canadian Geotechnical Journal*, 37:592–606, 2000.
- [37] T. Wichtmann. Explicit accumulation model for non-cohesive soils under cyclic loading. PhD thesis, Publications of the Institute of Soil Mechanics and Foundation Engineering, Ruhr-University Bochum, Issue No. 38.

- [38] T. Wichtmann, A. Niemunis, and T. Triantafyllidis. Strain accumulation in sand due to cyclic loading: drained triaxial tests. *Soil Dynamics and Earthquake Engineering*, 25(12):967–979, 2005.
- [39] T. Wichtmann, A. Niemunis, and T. Triantafyllidis. Experimental evidence of a unique flow rule of non-cohesive soils under high-cyclic loading. *Acta Geotechnica*, 1(1):59–73, 2006.
- [40] T. Wichtmann, A. Niemunis, and T. Triantafyllidis. Validation and calibration of a high-cycle accumulation model based on cyclic triaxial tests on eight sands. *Soils and Foundations*, 49(5):711–728, 2009.
- [41] T. Wichtmann, A. Niemunis, and T. Triantafyllidis. On the "elastic stiffness" in a high-cycle accumulation model - continued investigations. *Canadian Geotechnical Journal*, 50(12):1260–1272, 2013.
- [42] T. Wichtmann, A. Niemunis, and T. Triantafyllidis. Flow rule in a high-cycle accumulation model backed by cyclic test data of 22 sands. *Acta Geotechnica*, 9(4):695–709, 2014.
- [43] T. Wichtmann, A. Niemunis, T. Triantafyllidis, and M. Poblete. Correlation of cyclic preloading with the liquefaction resistance. *Soil Dynamics and Earthquake Engineering*, 25(12):923–932, 2005.
- [44] T. Wichtmann, A. Niemunis, and Th. Triantafyllidis. Differential settlements due to cyclic loading and their effect on the lifetime of structures. In F. Stangenberg, O.T. Bruhns, D. Hartmann, and G. Meschke, editors, *Proc. of 3rd Intern. Conf. on Lifetime-oriented Design Concepts, Bochum, 12 - 14 November*, pages 357–364. Aedificatio, 2007.
- [45] T. Wichtmann, A. Niemunis, and Th. Triantafyllidis. Towards the FE prediction of permanent deformations of offshore wind power plant foundations using a high-cycle accumulation model. In *International Symposium: Frontiers in Offshore Geotechnics, Perth, Australia*, pages 635–640, 2010.
- [46] D. Wijewickreme, S. Sriskandakumar, and P. Byrne. Cyclic loading response of loose air-pluviated Fraser River sand for validation of numerical models simulating centrifuge tests. *Canadian Geotechnical Journal*, 42:550–561, 2005.
- [47] V.C. Xenaki and G.A. Athanasopoulos. Liquefaction resistance of sand - silt mixtures: an experimental investigation of the effects of fines. *Soil Dynamics and Earthquake Engineering*, 23:183–194, 2003.
- [48] S. Yamada, T. Takamori, and K. Sato. Effects on reliquefaction resistance produced by changes in anisotropy during liquefaction. *Soils and Foundations*, 50(1):9–25, 2010.
- [49] S. Yamashita and S. Toki. Effects of fabric anisotropy of sand on cyclic undrained triaxial and torsional strengths. *Soils and Foundations*, 33(3):92–104, 1993.
- [50] J. Yang and H.Y. Sze. Cyclic behaviour and resistance of saturated sand under non-symmetrical loading conditions. *Géotechnique*, 61(1):59–73, 2011.
- [51] J. Yang and H.Y. Sze. Cyclic Strength of Sand under Sustained Shear Stress. *Journal of Geotechnical and Environmental Engineering, ASCE*, 137(12):1275–1285, 2011.
- [52] H. Zachert, T. Wichtmann, T. Triantafyllidis, and U. Hartwig. Simulation of a full-scale test on a Gravity Base Foundation for Offshore Wind Turbines using a High Cycle Accumulation Model. In *3rd International Symposium on Frontiers in Offshore Geotechnics (ISFOG), Oslo*, 2015.
- [53] J.-M. Zhang, Y. Shamoto, and K. Tokimatsu. Moving critical and phase-transformation stress state lines of saturated sand during undrained cyclic shear. *Soils and Foundations*, 37(2):51–59, 1997.
- [54] J.-M. Zhang and G. Wang. Large post-liquefaction deformation of sand, part I: physical mechanism, constitutive description and numerical algorithm. *Acta Geotechnica*, 7:69–113, 2012.